PHYSICAL REVIEW D **85,** 056010 (2012)

Density of states and Fisher's zeros in compact $U(1)$ pure gauge theory

A. Bazavov
Department of Physics, Brookhaven National Laboratory, Upton, New York 11973, USA

B. A. Berg
Department of Physics, Florida State University, Tallahassee, Florida 32306, USA

Daping Du
Physics Department, University of Illinois, Urbana, Illinois 61801, USA

Y. Meurice
Department of Physics and Astronomy, The University of Iowa, Iowa City, Iowa 52242, USA
(Received 15 February 2012; published 30 March 2012)

We present high-accuracy calculations of the density of states using multicanonical methods for lattice gauge theory with a compact gauge group $U(1)$ on 4^4, 6^4, and 8^4 lattices. We show that the results are consistent with weak and strong coupling expansions. We present methods based on Chebyshev interpolations and Cauchy theorem to find the (Fisher's) zeros of the partition function in the complex $\beta = 1/g^2$ plane. The results are consistent with reweighting methods whenever the latter are accurate. We discuss the volume dependence of the imaginary part of the Fisher's zeros, the width and depth of the plaquette distribution at the value of β where the two peaks have equal height. We discuss strategies to discriminate between first- and second-order transitions and explore them with data at larger volume but lower statistics. Higher statistics and even larger lattices are necessary to draw strong conclusions regarding the order of the transition.

DOI: 10.1103/PhysRevD.85.056010 PACS numbers: 11.15.−q, 11.15.Ha, 11.15.Me

I. INTRODUCTION

The ongoing effort at the Large Hadron Collider has triggered a renewed interest in the phase structure of lattice gauge theory models that may possibly provide an alternative to the Higgs mechanism of the electroweak symmetry breaking. In particular, the locations of the conformal windows for various families of models have stirred intense discussions. Different numerical and analytical techniques have been applied to QCD-like models with large numbers of fermion flavors [1–6] or with fermions in higher representations [7–12]. An interesting attempt to classify possible phases of such models based on an effective potential for the Polyakov loop was made in [13]. See also [14–16] for recent reviews of results and expectations. Another direction where massive vector bosons emerge without introducing new fermion species but in a model with modified gauge transformations has been pursued in [17,18].

In this context, it is important to understand the critical behavior of lattice models from as many consistent points of view as possible. Recently, it was proposed to consider complex extensions [19–21] of the framework proposed by Tomboulis [22] to explain confinement from the point of view of the renormalization group approach. A general feature that we observed is that the Fisher's zeros, the zeros of the partition function in the complex β plane [23], play an important role in the determination of the global properties of the complex renormalization group flows. In the case where a phase transition is present, the scaling properties of the zeros [24–29] allow us to distinguish between a first- and second-order phase transition.

Despite its apparent simplicity, the case of the four-dimensional pure gauge compact $U(1)$ model with a Wilson action is not completely free of controversy. The presence of a double peak for the plaquette distributions near $\beta \simeq 1$ suggests a first-order phase transition. However, if spherical lattices are considered, the double peak disappears [25,26]. In addition, finite size scaling, at relatively small volumes seems consistent with a second-order phase transition with an exponent $\nu \simeq 0.35$–0.40. On the other hand, a possible scenario [30] is that as the volume increases, ν slowly "rolls" towards the first-order value $\nu = 1/D = 0.25$. In the more recent literature [31–34], the idea that the transition is first order is favored. Using finite size scaling, the authors of Ref. [33] estimated the critical value $\beta_\infty = 1.011\,131\,0(62)$.

In this article, we introduce new methods to locate the Fisher's zeros of the four-dimensional pure gauge compact $U(1)$ model with a Wilson action. We rely on high-accuracy determinations of the density of states, a quantity defined in Sec. II, by multicanonical methods [35–38] presented in Sec. III. The lattice sizes considered are 4^4, 6^4, and 8^4. The consistency of the results with weak and strong coupling expansion is checked in Sec. IV. The density of states has a convex region which implies a double-peak plaquette distribution near $\beta \simeq 1$. The volume

dependence of the double-peak distribution is discussed empirically in Sec. V. In Sec. VI, Chebyshev interpolations of the logarithm of the density of states and Cauchy theorem are used to find the Fisher's zeros in the complex $\beta = 1/g^2$ plane. For the lowest zeros, it is possible to check consistency with reweighting methods within error bars estimated from the statistical fluctuations of 20 independent multicanonical streams.

In the following, we use very high statistics on rather small lattices, because this allows us to explore new analysis methods and to test whether they converge faster toward the infinite volume limit. We plan to use similar methods for $SU(2)$ where the imaginary parts of the lowest zeros are larger and reweighting methods become less reliable when the volume increases [39].

Using high statistics at small volumes (4^4, 6^4, and 8^4), we show that the imaginary part of the lowest zero appears to decrease like $L^{-3.08}$, when the linear size L increases from 4 to 8. This could be interpreted as signaling a second-order phase transition with $\nu = 0.325$, a value close to the estimates of Refs. [25,26]. However, using data at larger volumes but with lower statistics, we found indications for the ''rolling'' scenario of [30]. This is discussed in Sec. VII where we also consider volume effects on the width and depth of the plaquette distribution at the value of β where the two peaks have equal height. Simulations required to provide a clear-cut distinction between first- and second-order transitions are discussed in the Conclusions.

II. DENSITY OF STATES IN ABELIAN GAUGE THEORY

In the following, we consider the pure gauge partition function

$$Z = \prod_l \int \frac{d\theta_l}{2\pi} e^{-\beta S}, \tag{1}$$

with $\beta \equiv 1/g^2$ and the Wilson action

$$S = \sum_p (1 - \cos\theta_p). \tag{2}$$

We use D-dimensional symmetric cubic lattices with L^D sites and periodic boundary conditions. The number of plaquettes is denoted $\mathcal{N}_p \equiv L^D D(D-1)/2$. We define the average action:

$$P \equiv \langle \mathcal{S}/\mathcal{N}_p \rangle = -d(\ln Z/\mathcal{N}_p)/d\beta. \tag{3}$$

Inserting 1 as the integral of the delta function over S in Z, we can write

$$Z = \int_0^{2\mathcal{N}_p} dS n(S) e^{-\beta S}, \tag{4}$$

with the density of states defined as

$$n(S) = \prod_l \int dU_l \delta\Big(S - \sum_p (1 - \cos\theta_p)\Big). \tag{5}$$

Furthermore, we introduce the notation s for $S/\mathcal{N}_p$ and we define the entropy density $f(s)$ via the equation

$$n(S) = e^{\mathcal{N}_p f(S/\mathcal{N}_p)}. \tag{6}$$

A more general discussion for spin models [40] or gauge models [41] can be found in the literature where the density of states is sometimes called the spectral density. From its definition, it is clear that $n(S)$ is positive. Assuming that the measure for the links is normalized to 1, the partition function at $\beta = 0$ is 1. It can be shown [42] that, if the lattice has even number of sites in each direction, and if the gauge group contains $-\mathbb{1}$, then $\beta\cos\theta_p$ goes into $-\beta\cos\theta_p$ by a change of variables $\theta_l \rightarrow \theta_l + \pi$ on a set of links such that for any plaquette, exactly one link of the set belongs to that plaquette. Using

$$Z(-\beta) = e^{2\beta\mathcal{N}_p} Z(\beta), \tag{7}$$

we find the duality

$$n(2\mathcal{N}_p - S) = n(S). \tag{8}$$

This implies the reflection symmetry

$$f(s) = f(2 - s). \tag{9}$$

Numerical values of $f(s)$ have been obtained for discrete values of s between 0 and 1. When s is close to 0 or 2, $f(s)$ diverges logarithmically and we can only reach values of s that are not too close to 0 or 2. Consequently, the results cannot be used if $|\beta|$ is too large. Using the symmetry Eq. (9) and interpolation methods, a continuous function can be obtained in an interval $[\delta, 2 - \delta]$, where δ is an appropriately small quantity.

III. CALCULATION OF THE DENSITY OF STATES

We performed Monte Carlo simulations in pure $U(1)$ gauge theory using biased Metropolis-heatbath updates [37]. To cover a large range of couplings $\beta \in [0, 9]$, we used the multicanonical (MUCA) algorithm [35] with Wang-Landau recursion [36] for the multicanonical weights. The software we used is described in Ref. [38].

We generated large statistics on symmetric lattices with volumes 4^4, 6^4, and 8^4. After the initial recursion, we performed three MUCA runs on 4^4, and two runs on 6^4 and 8^4. The first MUCA run on 4^4 was regarded as exploratory and we did not include it in the final analysis. The weights for each next run were refined from the previous run. In total, we used 20 independent streams for each lattice volume. In each stream, we ran Wang-Landau recursion for the multicanonical weights before the production, therefore the weights differ between the streams, $w_{ij}(S)$, where S is the total action, $i = 1, \ldots, 20$ denotes different streams and $j = 1, 2$ denotes MUCA runs.

The quality of a MUCA run is indicated by the number of tunneling events (i.e., how often during a run the system

travels from the lowest energy to the highest and back). Also, to estimate how many statistically independent events we generated, we measured the integrated autocorrelation times. These data are summarized in Appendix A. Our statistics consists of $N_{\rm equi}$ sweeps for equilibration and $N_{\rm rpt} = 64 \times N_{\rm equi}$ sweeps for measurements, where $N_{\rm equi} = 10^6$ for 4^4 and 6^4 lattices and 8×10^5 for 8^4.

For the error analysis, we considered two MUCA runs in each stream as independent measurements. Thus, on each lattice we had 40 independent measurements in total. For all quantities in the following, the error bars are estimated from an uncorrelated average of these 40 measurements, weighted with the number of tunneling events in each corresponding run, since runs with more tunnelings sample the density of states better. The average results for $f(s)$ are shown in Fig. 1.

To reweight an observable to the canonical ensemble, we need to cancel the multicanonical weight $w_{ij}(S)$ and replace it with the Boltzmann factor $\exp(-\beta S)$. For an observable $\mathcal{O}$ of interest, for instance, plaquette, we reweight the time series accumulated during a MUCA run ij to a given coupling β:

$$\langle O\rangle_{ij}(\beta) = \frac{\sum_{k=1}^{N_{\rm rpt}} O_{ij}^k \exp(-\beta S_{ij}^k)/w_{ij}(S_{ij}^k)}{\sum_{k=1}^{N_{\rm rpt}} \exp(-\beta S_{ij}^k)/w_{ij}(S_{ij}^k)}. \tag{10}$$

The final average is then given as

$$\langle O\rangle(\beta) = \frac{\sum_{i=1}^{20}\sum_{j=1}^{2} N_{ij}^{\rm tunn}\langle O\rangle_{ij}(\beta)}{\sum_{i=1}^{20}\sum_{j=1}^{2} N_{ij}^{\rm tunn}}, \tag{11}$$

where the number of tunnelings $N_{ij}^{\rm tunn}$ is given in Appendix A.

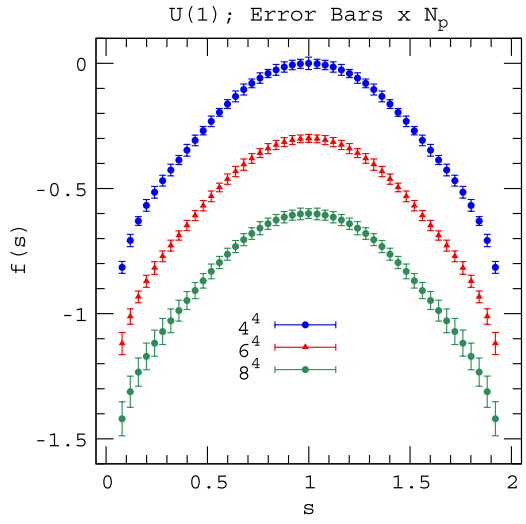

FIG. 1 (color online). $f(s)$ on a 4^4 (top), 6^4 (middle), and 8^4 (bottom) lattices; the errors have been multiplied by $\mathcal{N}_p$; for readability, arbitrary constants have been added to separate the data sets and only one of every 40 points is displayed.

IV. CONSISTENCY WITH EXISTING RESULTS AND EXPANSIONS

A. Comparison with the average plaquette

As a check of consistency, we compared the average plaquette at various β, as obtained directly from the runs, Eq. (11), and calculated using the average density of states. As shown in Fig. 2, there is a good agreement within the estimated errors.

B. Series for $f(s)$

We compared the numerical results for $f(s)$ with analytical results obtained using the weak and strong coupling expansions. The general methodology has been discussed for $SU(2)$ in [43] and remains applicable here. The basic ingredient is the saddle point equation at s_0:

$$f'(s_0) = \beta, \tag{12}$$

which can be used to convert an expansion of f in powers of s (or $(s-1)^2$) into an expansion of s_0 in powers of $1/\beta$ (or β, respectively). The coefficients of f can then be determined whenever the appropriate expansion of the average plaquette is available. In order to take the finite volume effects into account, we need to include at least the lowest-order volume correction, namely,

$$P = s_0 + (1/2\mathcal{N}_p)(f'''(s_0)/(f''(s_0))^2) + \mathcal{O}(1/\mathcal{N}_p^2). \tag{13}$$

Using Eqs. (12) and (13) together with an existing expansion of P including $1/\mathcal{N}_p$ effects up to a certain order, one can determine the coefficients of f up to the corresponding order.

It should also be noted that at finite volume, there is a finite range of β for which f' has a "Maxwellian kink" (discussed in Sec. VII) and three solutions of Eq. (12) are available rather than one. In this region, both expansions are expected to fail. We now proceed to discuss them separately.

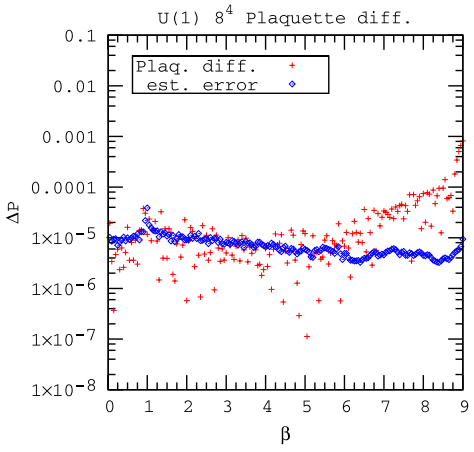

FIG. 2 (color online). Difference between the average plaquette calculated with the density of states and directly, for a 8^4 lattice.

C. Strong coupling

Following Ref. [43], we define

$$g(y) \equiv f(1+y) \equiv \sum_{m=0} g_{2m} y^{2m}. \tag{14}$$

Using saddle point approximation and comparing, order by order, with the expansion of the average plaquette from the strong coupling expansion [44], we can determine the expansion of $g(y)$. As in the case of $SU(2)$, there are logarithmic singularities at $y = \pm 1$, which can be subtracted by defining

$$h(y) \equiv g(y) - A\ln(1-y^2) \equiv \sum_{m=0} h_{2m} y^{2m}. \tag{15}$$

The value of A comes from the weak coupling expansion and will be discussed in the next subsection [see Eq. (20)]. The infinite volume results are summarized in Table I. The entries make clear that as the order increases, the effect of the logarithmic subtractions becomes smaller. This indicates singularities closer to $y = 0$ ($s = 1$).

The improvement of the approximation with successive order is shown in Fig. 3. The graph shows that for $s \gtrsim 0.5$, successive orders provide better approximations up to the point where the numerical accuracy is reached. Such a range corresponds to a convergent region $\beta \lesssim 0.9$ in the β plane.

It should be noted that for the strong coupling expansion, the finite volume effects are negligible for $V = 8^4$. Indeed, they are even hard to resolve for $V = 4^4$. This can be traced to the fact [43] that even for this volume, the dependence on V would appear at order β^8 from the contributions of strong coupling graphs called torelons [45] that wrap around the periodic volume in one direction. As translations in that direction do not generate new graphs, such graphs have a suppression of order $1/L$ compared to graphs with a trivial topology. Consequently, for order less than 8, the finite volume effects can be estimated by canceling the volume dependence in the two terms of the right-hand side of Eq. (13). For instance, at lowest order, we find that

TABLE I. $U(1)$ strong coupling expansion coefficients a_{2m} of P (rescaled from Ref. [44]), and of $f(s)$ defined in the text.

m	a_{2m}	g_{2m}	h_{2m}
1	$-\frac{1}{2}$	-1	$-\frac{3}{4}$
2	$\frac{1}{16}$	$-\frac{1}{4}$	$-\frac{1}{8}$
3	$-\frac{13}{96}$	$\frac{43}{36}$	$\frac{23}{18}$
4	$\frac{779}{6144}$	$-\frac{19}{192}$	$-\frac{7}{192}$
5	$-\frac{11819}{61440}$	$-\frac{7343}{1800}$	$-\frac{7253}{1800}$
6	$\frac{2017373}{847360}$	$\frac{465331}{25920}$	$\frac{466411}{25920}$
7	$-\frac{20224291}{123863040}$	$-\frac{983357143}{1693440}$	$-\frac{983296663}{1693440}$
8	$\frac{5775175013}{12683575296}$	$-\frac{201757201579}{46448640}$	$-\frac{201755750059}{46448640}$

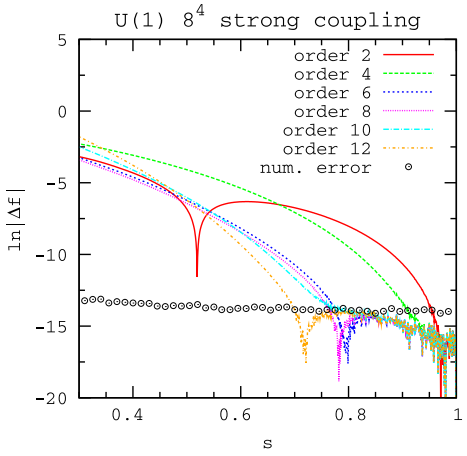

FIG. 3 (color online). Natural logarithm of the absolute value of the difference between $f(s)$ calculated on a 8^4 lattice and successive approximations obtained from the strong coupling expansion.

$$g_2 = -1 + 1/(8V). \tag{16}$$

Consequently, the difference $\Delta f(s)$ of $f(s)$ for two different volumes V_1 and V_2 near $y = 0$ ($s = 1$) is

$$\Delta f(s) \simeq (1/8)(1/V_1 - 1/V_2)(s-1)^2. \tag{17}$$

Even for $V = 4^4$, this difference is smaller than the error bars in the region $s \simeq 1$. In order to reduce the noise, we have averaged the data in bins of ten data points. The results are displayed in Fig. 4 which shows that the data and the analytical result in Eq. (17) are compatible.

D. Weak coupling

A similar approach can be followed in the weak coupling limit. At small s, the logarithmic singularity dominates and we assume that

$$f(s) = A\ln(s) + \sum_{m=0} f_m s^m. \tag{18}$$

The unknown coefficients can be determined from the weak coupling expansion of the average plaquette

$$P \simeq \sum_{m=1} b_m \beta^{-m}. \tag{19}$$

The volume-dependent coefficients b_m have been calculated up to order 4 in Ref. [46]. The two lowest orders of the expansion can be performed exactly and yield

$$A = 1/4 - 5/(12V), \tag{20}$$

$$f_1 = (1/8)(1 - 1/V). \tag{21}$$

The higher orders involve numerical loop calculations. The results of the expansion as well as the volume corrections for the 4^4 and 6^4 lattices are shown in Table II.

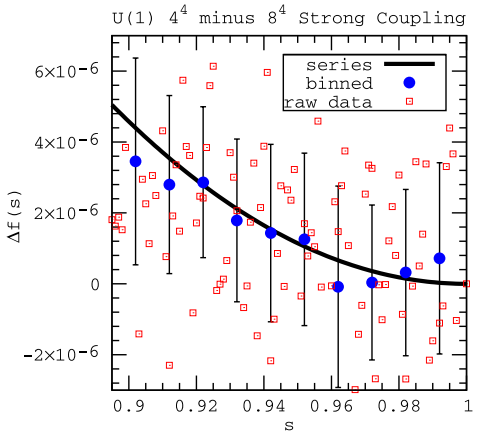

FIG. 4 (color online). Difference between $f(s)$ on 4^4 and 8^4 near $s = 1$ (boxes). The circles are obtained by averaging over bins of size 10. The solid line is Eq. (17). The part with $s > 1$ can be obtained by symmetry and is not shown.

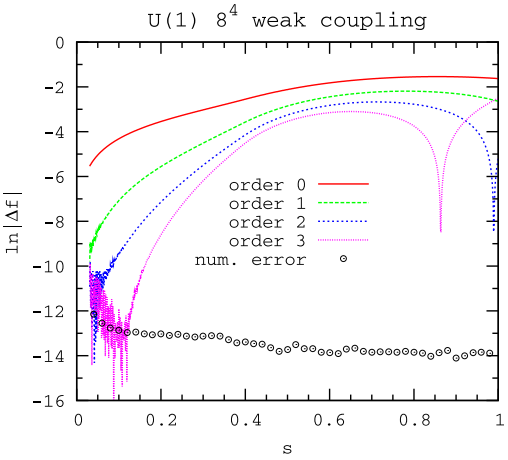

FIG. 5 (color online). Difference between $f(s)$ calculated on a 8^4 lattice and successive approximations obtained from the weak coupling expansion.

The difference between numerical and analytical results is shown in Fig. 5 for $V = 8^4$. The graph makes it clear that the quality of the approximation increases as three successive corrections to the leading logarithm are added. The third correction is good enough to reproduce the data within the numerical accuracy for $s < 0.1$. This order is not sufficient to identify a "nonperturbative envelope" defined in Ref. [47] and observed for $SU(2)$ in Ref. [43].

The difference between $V = 4^4$ and $V = 8^4$ is shown in Fig. 6. Note that for the smallest volume ($V = 4^4$), the resolution in s used during the multicanonical simulation is coarser than the 1000 bins used to represent $f(s)$. Consequently, some small "staircase" structure appears near 0 where $f(s)$ changes rapidly. For this reason, we have averaged $f(s)$ over bins of size 10 and Fig. 6 shows a good agreement with the analytical expansion that includes the logarithmic singularity and a linear term. Higher-order corrections are significantly smaller than the errors bars. There is an arbitrary constant in the expansion of $f(x)$ which cannot be determined by the saddle point equation. For the numerical data, such a constant may differ for two different volumes and needs to be subtracted.

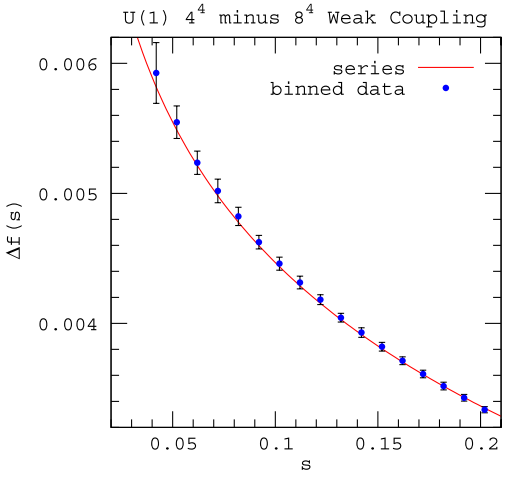

FIG. 6 (color online). Difference between $f(s)$ on 4^4 and 8^4 near $s = 0$ with average over bins of size 10. The solid line is the expansion described in the text.

TABLE II. The weak coupling expansion for $V = \infty$, 4^4, and 6^4. The upper half is the list of the expansion coefficients of the average plaquette P with respect to $1/\beta$ [46]. The lower half is the corresponding list of expansion coefficients of $f(x)$.

	$V = \infty$	$V = 6^4$	$V = 4^4$
b_1	$\frac{1}{4}$	$\frac{1295}{5184}$	$\frac{255}{1024}$
b_2	$\frac{1}{32}$	$\frac{2171747375}{208971104256}$	$\frac{65025}{2097152}$
b_3	0.013 11	0.013 09	0.012 96
b_4	0.007 52	0.007 49	0.007 39
A	$\frac{1}{4}$	$\frac{3883}{15552}$	$\frac{763}{3072}$
f_1	$\frac{1}{8}$	$\frac{1295}{10368}$	$\frac{255}{2048}$
f_2	0.073 63	0.073 59	0.073 14
f_3	0.076 38	0.076 05	0.075 15

V. VOLUME DEPENDENCE IN THE CROSSOVER REGION

A. Empirical parametrization

The difference of $f(s)$ for 4^4 and 8^4 resembles the effective potential for the central Coulomb potential with a leading singularity near $s = 0.35$ and a $1/s$ behavior at larger s. Using in addition a constant that has no particular meaning as long as we do not normalize the density of states and a $1/s^2$ correction, we performed a 4-parameter fit with the 311 bins corresponding to $0.39 < s < 0.7$. The numerical result is

$$f(s) = -0.001\,120\,63 + 4.826\,41 \times 10^{-6}/(-0.35 + s)^2 - 0.000\,680\,501/s^2 + 0.001\,728\,82/s. \quad (22)$$

As shown in Fig. 7, it fits the data reasonably well.

B. Volume dependence of the double peak

The plaquette distributions for the volumes considered here have a double-peak structure for β near 1. At finite volume, it is easy to locate the value of β, denoted β_S hereafter, where the two peaks of $f(s) - \beta_S s$ have equal height. Other pseudocritical β have been defined in the literature [30,48–50]. The accuracy of the determination of β_S depends on the smoothness of the distribution and the size of the error bars. In Fig. 8, we show that $f(s) - \beta s$ is slightly tilted to the left for $\beta = 1.001\,75$ and to the right for $\beta = 1.001\,79$. Given the smoothness of the distribution, we conclude that $\beta_S = 1.001\,77(2)$. With the same graphs, we can also determine approximate values of the two maxima s_1 and s_2. The numerical results for the three volumes considered are provided in Table III.

The density of states can be used to calculate the plaquette probability distribution at β_S. The results are shown in Fig. 9 where the normalization has been chosen in such a way that the integral under the curve is approximately one. Figure 9 makes it clear that the dip between the peaks deepens and the peak separation decreases as the volume increases. This will be discussed in more detail in Sec. VII.

VI. FISHER'S ZEROS

A. Approximate zeros from reweightings

Approximate values of Z at fixed β can be obtained by using the Riemann sum approximations of Eq. (4):

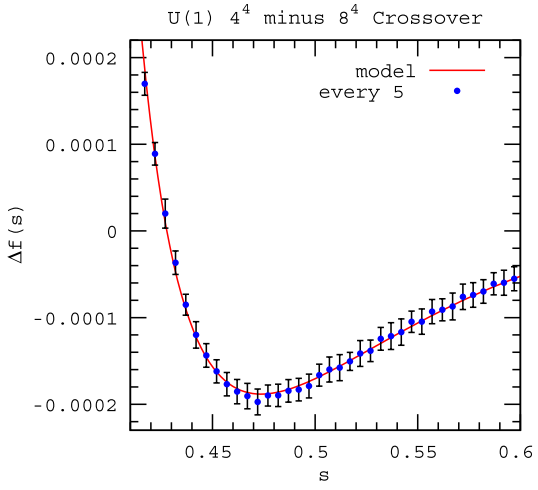

FIG. 7 (color online). Difference between $f(s)$ on 4^4 and 8^4 near $s = 0.5$. For readibilty, we only show every 5 points (no binning). The solid line is the fit given in Eq. (22).

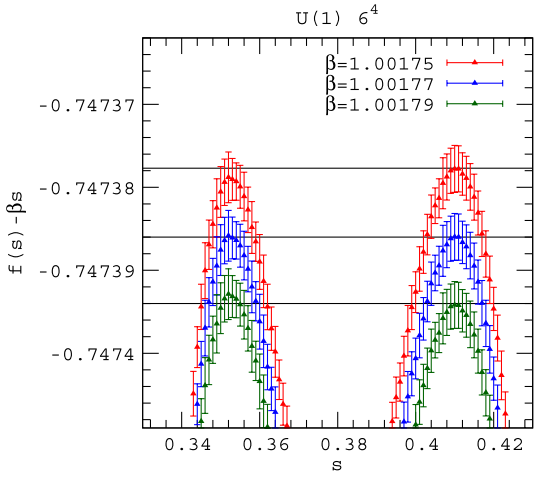

FIG. 8 (color online). $f(s) - \beta s$ for $\beta = 1.001\,75$, $100\,177$, and $1.001\,79$ on a 6^4 lattice. The horizontal lines have been drawn to emphasize small height asymmetries.

TABLE III. β_S, s_1, and s_2 defined in the text for $L = 4$, 6, and 8.

L	β_S	s_1	s_2
4	0.9793(1)	0.370(5)	0.445(5)
6	1.001 77(2)	0.353(2)	0.411(2)
8	1.007 34(1)	0.349(1)	0.395(1)

$$Z(\beta) \simeq \Delta s \sum_s e^{\mathcal{N}_p(f(s)-\beta s)}. \quad (23)$$

We can now study how the error δf on $f(x)$ can affect our estimates of Z. The relevant quantity $\mathcal{N}_p \delta f$ is included in Fig. 1. For the three volumes, $\mathcal{N}_p \delta f$ is of the order of a few percents and linearization is justified. Small scale fluctuations of the same order are visible in the distributions of the independent streams.

As we are interested in locating Fisher's zeros, it is clear that the errors have a potentially important effect near an approximate zero. The best we can do is to identify regions where $|Z|$ is significantly larger than $|\delta Z|$ so that we can confidently say that there are no zeros in these regions. If we use the linear estimate

$$\delta Z(\beta) \simeq \Delta s \sum_s \mathcal{N}_p \delta f(s) e^{\mathcal{N}_p(f(s)-\beta s)}, \quad (24)$$

we have the inequality

$$|\delta Z(\beta)| < \Delta s \sum_s \mathcal{N}_p |\delta f(s)| e^{\mathcal{N}_p(f(s)-\mathrm{Re}\beta s)}, \quad (25)$$

but in general the bound is not sharp because the sign of $\delta f(s)$ can vary rapidly. We have estimated $|\delta Z|$ by taking the difference between Z calculated with the averaged f and Z calculated with the stream with the most tunnelings. The results are shown in Fig. 10. A mesh of 0.000 25 in β is

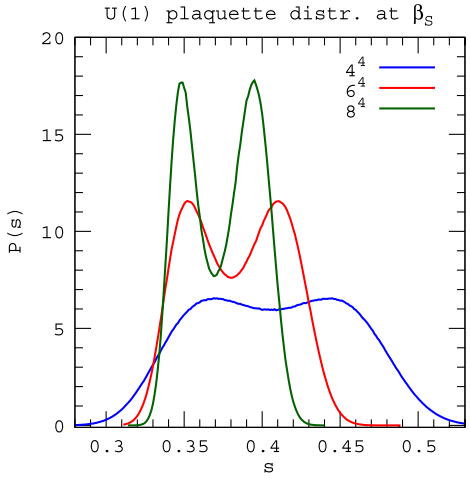

FIG. 9 (color online). Plaquette distribution for $U(1)$ at β_S for $L = 4$, 6, and 8.

used which is larger than the typical fluctuations in f. The light (toward yellow online) regions represent the areas where we cannot exclude zeros. The dark (toward blue online) regions represent the areas where zeros are very unlikely. A small light region is an indication for the existence of a zero while a broad light region indicates that the errors dominate. The second possibility typically appears at large imaginary β where due to rapid oscillations of the integrand, cancellations occur making the final results more sensitive to the errors on $f(s)$. In view of this remark, Fig. 10 suggests that reweighting methods allow to estimate the locations of the two lowest zeros for $L = 4$ and three lowest zeros for $L = 6$.

We have also calculated ReZ and ImZ from Eq. (23) using the average f. Their respective zeros are shown in Fig. 11. The complex zeros appear at the intersections of the two sets of curves defined by Re$Z = 0$ and Im$Z = 0$, respectively. This happens in a way which is consistent with Fig. 10. Error bars can be estimated by comparing the intersections for the 20 streams. The results are given in Tables IV and V.

B. Chebyshev interpolations

The original grids of the density of states are sometimes not sufficient for precise numerical integrations which is how we define our partition function. It is especially true when the imaginary component of β is large and, as a consequence, the partition function oscillates more frequently than the original grids can resolve. It is convenient to apply the Chebyshev interpolation which provides arbitrary integrating step sizes for designed integral precision. For the Chebyshev interpolation of numerical data, the determination of the coefficients by the least square fit method is more efficient and robust than by discrete or integration methods. In this paper, we will primarily follow this approach.

A range of interest $[a, b]$ can be mapped to $[-1, 1]$ in which we express the target function by

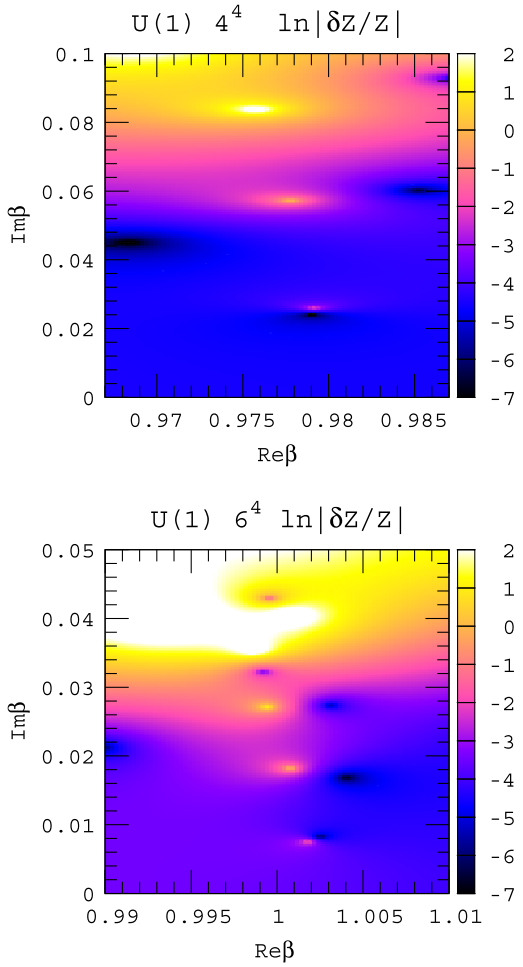

FIG. 10 (color online). $\ln|\delta Z/Z|$ for 4^4 and 6^4 lattices.

$$f(y) = \sum_{n=0}^{N_c} c_n T_n(y). \tag{26}$$

We then minimize the distance of the function to a data set or multiple data sets, which will uniquely determine the coefficients c_n of linear equations.

We shall keep in mind that, like other polynomial approximations, Chebyshev interpolations may introduce artifacts such as fake zeros. We want to make sure that the true zeros are distinct from the fake ones. Special attention should be paid to the range of approximation. In practice, we often use a small range to emphasize the numerical signal from a certain region. The average plaquette $\langle x \rangle$ is related to the coupling β, through $\langle x \rangle_\beta = -\partial \ln Z(\beta)/\partial\beta/\mathcal{N}_p$. This is not valid if $\langle x \rangle$ goes beyond the range of the approximation (an ellipse in the complex plane, see below). Reducing the range of interpolation may introduce fake zeros with large Imβ in the β complex plane. However, the lowest zeros are usually not affected. Care should also be paid on the orders of the Chebyshev approximation. True zeros should be independent of the order of polynomials. In the following, we always use

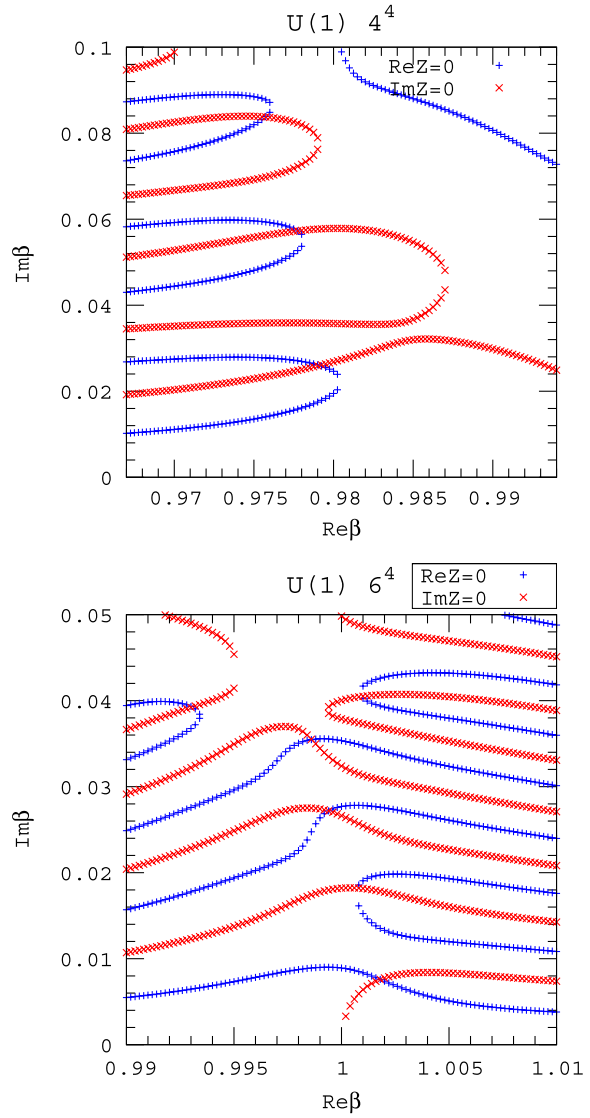

FIG. 11 (color online). Zeros of the Re (+ , blue online) and Im (x, red online) part of Z for $U(1)$ using the density of states for 4^4 and 6^4 lattices.

various orders of Chebyshev interpolations and make sure that the zeros are free of these artifacts.

C. Ellipse of convergence

The definition

$$T_n(z) = \cos(n \arccos(z)) \tag{27}$$

shows that the expansion in Chebyshev polynomials is a Fourier expansion for the variable $\arccos(x)$. If $|c_{n+1}/c_n|$ from Eq. (26) reaches a limit C, then the expansion converges for $|T_n(z)| < C^{-n}$. To work on the complex plane, the following relation is helpful: $T_n(z) = (\omega^n + \omega^{-n})/2$, when z is expressed as $z = (\omega + \omega^{-1})/2$. The convergence of a Chebyshev series is then analyzed through the variable ω. It can be shown [51] that the region of convergence on the ω plane is a ring confined by a pair of concentric circles and the region is mapped into an area bounded by an ellipse on the z plane.

The continuation of the Chebyshev expansion to the complex plane is limited by the ellipse. Fortunately, in the case of $U(1)$, the lowest complex zeros are typically very close to the real axis and these zeros are well inside the ellipse of convergence.

TABLE IV. Real part of the first three zeros.

L	First	Second	Third
4	0.9791(1)	0.9780(4)	Not stable
6	1.001 80(5)	1.0007(1)	0.9993(5)
8	1.007 44(2)	1.0068(2)	1.0061(4)

TABLE V. Imaginary part of the first three zeros.

L	First	Second	Third
4	0.0259(1)	0.057(1)	Not stable
6	0.007 58(2)	0.018(1)	0.027(2)
8	0.003 06(2)	0.008(1)	0.012(1)

D. Locating zeros with the residue theorem

There is a general algorithm to find the zeros of an analytic function by using Cauchy's integral theorem [52]. For simplicity, we will only consider the special case when all the zeros are of order 1 which apparently applies to our problem. Suppose that an analytic function $Z(\beta)$ has K zeros enclosed by a closed contour C, then

$$\frac{1}{2\pi i}\oint_c (\ln Z)'\beta^n d\beta = \sum_{i=1}^{K}(\beta_i)^n, \qquad n = 0, 1, 2, \ldots \tag{28}$$

where β_i are all the zeros in contour C. When $n = 0$, the summation on the right-hand side is just the number of zeros.

The partition function we are considering is an analytic function, since it is just a sum of analytic functions. We scan the complex plane with rectangular contours which enclose two or less zeros. We monitor the $n = 0$ integral which should give the number of zeros very close to an integer and a very small imaginary part. The method turns out to be quite robust and reliable.

E. Zero structure near the real axis

The lowest zeros from three volumes are given in Table VI and shown in Fig. 12. The error bars take into account both the Monte Carlo statistical error and the (much smaller) Chebyshev interpolation error. The three lines are the linear fits for the first, second, and third lowest zeros. They intersect the real axis approximately at the same point $\beta = 1.011\,34(1)$. Figure 12 also shows that β_S and the real part of the zeros are highly correlated.

The good look of the linear fits is deceptive as they have a rather large χ^2 and a small goodness of fit Q (see p. 111

TABLE VI. The lowest three zeros in the volumes 4^4, 6^4, and 8^4. Columns 2–4 are the real parts of the zeros, the estimate error σ_s from different streams of Monte Carlo runs and the error σ_c due to the orders of Chebyshev interpolation (we used three different orders 40, 44, and 50 for all three volumes). Columns 5–7 are similar quantities for the imaginary parts.

L	Reβ	σ_s	σ_c	Imβ	σ_s	σ_c
	0.979 123 5	3.6×10^{-5}	5.3×10^{-8}	0.026 006 5	3.7×10^{-5}	3.9×10^{-9}
4	0.977 731 4	3.5×10^{-4}	7.1×10^{-6}	0.057 276 4	1.4×10^{-4}	3.3×10^{-6}
	0.975 295 4	1.1×10^{-3}	2.9×10^{-4}	0.083 170 5	1.3×10^{-3}	3.2×10^{-4}
	1.001 796 9	1.7×10^{-5}	1.7×10^{-6}	0.007 582 1	8.7×10^{-6}	1.4×10^{-6}
6	1.000 743 3	6.0×10^{-5}	2.3×10^{-5}	0.018 204 4	2.8×10^{-5}	4.0×10^{-6}
	0.998 896 4	1.4×10^{-4}	2.7×10^{-4}	0.027 186 6	4.5×10^{-4}	1.5×10^{-4}
	1.007 438 0	1.1×10^{-5}	7.7×10^{-8}	0.003 065 3	3.6×10^{-6}	6.8×10^{-8}
8	1.006 829 6	2.3×10^{-5}	2.1×10^{-6}	0.007 767 3	2.4×10^{-5}	3.3×10^{-7}
	1.006 041 0	1.1×10^{-4}	1.2×10^{-5}	0.011 507 9	1.0×10^{-4}	8.5×10^{-5}

of [53]) which can be explained by the small errors bars. Another potentially deceptive result is that the imaginary part of the lowest zero decreases like $L^{-3.08}$. If this result is indicative of what happens at larger volume, this would be interpreted as signaling a second-order phase transition with $\nu \simeq 1/3.08 \simeq 0.325$. Larger lattices are needed as will be discussed in Sec. VII.

F. Dependence on the range of integration

In the previous calculations, the tails of integration play a marginal role. If we are interested only in the zeros near $\beta = 1$, the density of states in a finite range is sufficient. This information becomes very important at higher volumes where the calculation is more expensive. In Table VII, we provide the values s_a and s_b outside of which the knowledge of $f(s)$ has effects smaller than the error bars on the zeros.

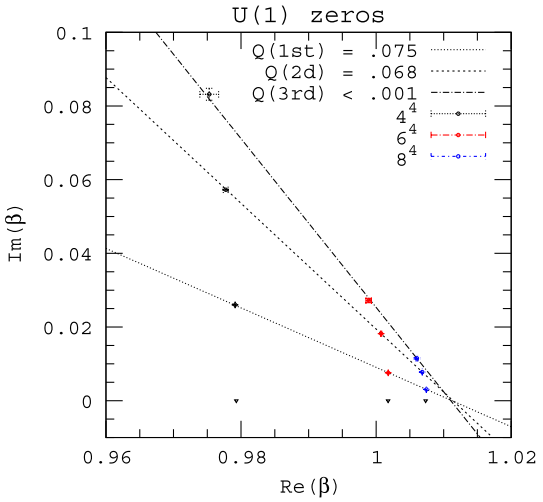

FIG. 12 (color online). The lowest zeros from the volumes 4^4, 6^4, and 8^4 (from left to right). Linear fits for the first, second, and third zeros (bottom to top) and their goodness of fit Q. The diamonds on the real axis are the double-peak β's from Table III.

VII. TOWARD LARGER VOLUME CALCULATIONS AND SCALING

In this section, we explore ways of discriminating between first- and second-order transitions. For this purpose, we include data at larger volumes ($L = 10$, 12, 14, and 20) from Ref. [54] with much lower statistics, namely, one stream with two MUCA runs.

A. Zeros

In Sec. VI, we explained that for the data for $L = 4$, 6, and 8, the imaginary part of the lowest zeros scales like $L^{-3.08}$. It is possible that as the volume increases, the approach of the real axis rolls toward the L^{-4} scaling expected for a first-order transition [30]. We now discuss the scaling of the zeros using the lower statistics data for the larger volumes given in Table VIII.

It is questionable that two MUCA runs could lead to a reliable estimate of the errors. An error bar from just two independent measurements fluctuates strongly and reaches a 95% confidence range only at about 14 (instead of 2) error bars (see p. 78 of [53]). We decided therefore to smoothen the error bars by assuming that the real relative error is the same for all four of our large lattices. Averaging these relative errors and multiplying them by three, the approximate 95% confidence range of four independent data gives an error bar of 1.69%, which is then given in the fourth column for all the large data of Table IX. Not to overweight the far more accurate small lattice against the large lattice data in the subsequent fits, they are also used with a relative error of 1.69% and thus listed in Table IX.

TABLE VII. Values of s_a and s_b and the corresponding values of β ($P(\beta) = s$).

L	s_a	s_b	β_a	β_b
4	0.274	0.488	1.125	0.945
6	0.284	0.436	1.1	0.985
8	0.295	0.408	1.075	1

TABLE VIII. Higher-volume zeros. Columns 2 and 4 are the averages over the two MUCA runs. Columns 3 and 5 are one-half of the differences (not the estimated error, see text).

L	Reβ	Δ Re/2	Imβ	Δ Im/2
10	1.009 47	2×10^{-5}	0.001 478	2×10^{-6}
12	1.010 27	2×10^{-5}	0.000 795	2×10^{-6}
14	1.010 64	2×10^{-5}	0.000 449	8×10^{-6}
20	1.011 01	1×10^{-5}	0.000 119	1×10^{-6}

We want to emphasize that this procedure has been designed to understand how different fits allow to discriminate between first and second order rather than to extract accurate values for the fitted parameters.

For these data, we performed 3-parameter fits, which are listed in the following together with their goodness of fit Q:

$$y = \frac{a_1}{L^4}\left(1 + \frac{a_2}{L} + \frac{a_3}{L^2}\right), \qquad Q = 0.43, \tag{29}$$

$$y = a_1 L^{a_2}\left(1 + \frac{a_3}{L}\right), \qquad Q = 6.2 \times 10^{-4}, \tag{30}$$

$$y = \frac{a_1}{L^4}\left(1 + a_2 L^{a_3}\right), \qquad Q = 2.8 \times 10^{-3}. \tag{31}$$

The first fit shows that L^{-4} behavior is consistent with all the data put together. The other two fits are in disagreement with the data.

Using *only* the data from the $L = 4, 6, 8$ lattices with the *modified* error bars given in Table IX, the 2-parameter fit

$$y = a_1 L^{a_2}, \qquad Q = 0.39 \tag{32}$$

is also in agreement with the data and gives the exponent $a_2 = -3.082(35)$ instead of -4. The fits (29) and (32) are shown in Fig. 13.

However, the fit

$$y = \frac{a_1}{L^{3.08}}\left(1 + \frac{a_2}{L} + \frac{a_3}{L^2}\right), \tag{33}$$

with the seven data points leads to $Q < 10^{-8}$. In addition, if we perform a four-parameter fit as in Eqs. (29) and (33) but with the leading exponent fitted, we obtain 4.121(74) for this exponent with $Q = 0.72$. These results seem to favor

TABLE IX. $y = \mathrm{Im}z$ from two independent runs on $L \geq 10$ lattices and their combination as explained in the text together with reduced accuracy values from $L \leq 8$ lattices.

L	First run	Second run	Combined
4	···	···	0.026 91 (44)
6	···	···	0.007 58 (13)
8	···	···	0.003 065 (52)
10	0.001 475 6	0.001 479 7	0.001 478 (25)
12	0.000 792 7	0.000 796 9	0.000 795 (14)
14	0.000 457 47	0.000 441 57	0.000 449 5 (76)
20	0.000 011 882	0.000 011 901	0.000 011 89 (21)

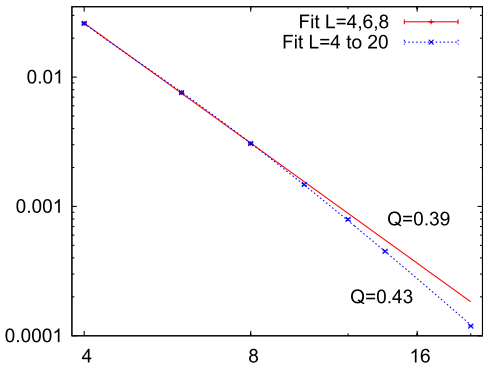

FIG. 13 (color online). Fits of Im$z(L)$ on a log-log scale.

the first-order possibility. However, they should be checked with higher statistics data for the larger volumes.

B. Features of $f(s)$

In the infinite volume limit, the width of the double-peak distribution goes to a nonzero limit (latent heat) for a first-order phase transition. For a second-order transition, this width should go to zero as an inverse power of L. These two possibilities are tested by plotting the width versus $1/L$ or in a log-log scale in Fig. 14.

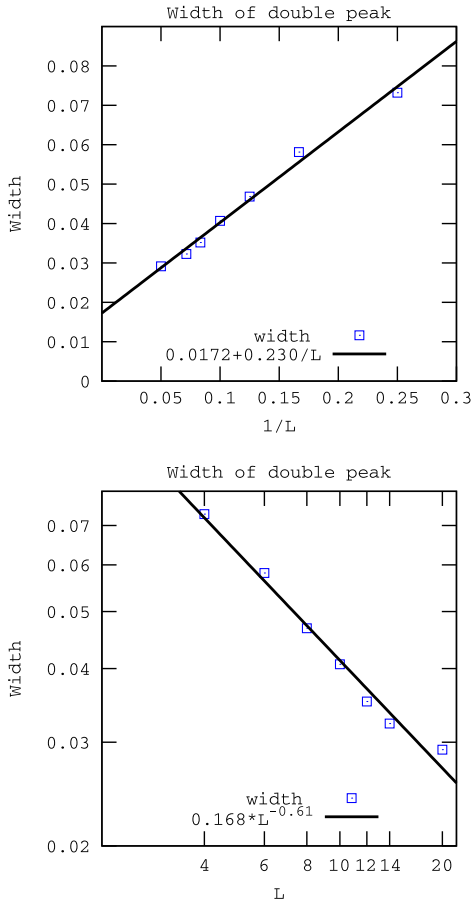

FIG. 14 (color online). Width of $f - \beta_S s$ as a function of L.

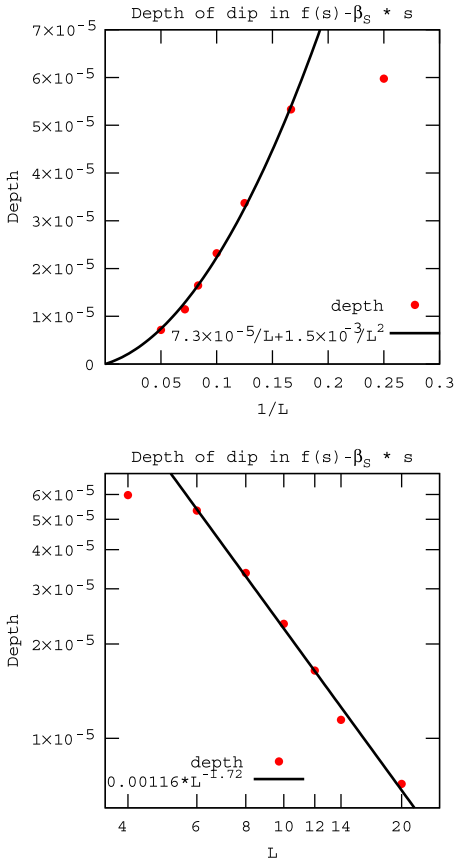

FIG. 15 (color online). Difference between the local minimum and the local maxima of $f - \beta_S s$ as a function of L.

The difference between the local minimum and the local maxima of $f - \beta_S s$ (by definition of β_S, the two local maxima have the same height) should decay like C/L for a first-order transition with C proportional to the interface tension. For a second-order transition, this difference should go to zero as an inverse power of L. The data is shown versus $1/L$ and on a log-log scale together with simple fits (made without $L = 4$) in Fig. 15. In the first fit, the $1/L^2$ corrections are clearly important and it is not surprising that the power in the second fit is between -1 and -2.

Using arguments from Ref. [55] leads to the conclusion that for a second-order phase transition, the width should scale like $L^{-(1-\alpha)/\nu}$, while the depth should scale like L^{-D}. If we use $D = 4$, $\nu \simeq 0.325$, and the hyperscaling relation $\alpha = 2 - D\nu \simeq 0.7$, we obtain $(1 - \alpha)/\nu \simeq 0.92$ which is not too far off for the width but very far off for the depth.

VIII. CONCLUSION

Using multicanonical methods, we have calculated the density of states for pure $U(1)$ lattice gauge theory with high precision on small 4^4, 6^4, and 8^4 lattices and with moderate precision on larger 10^4, 12^4, 14^4, and 20^4 lattices. From these data, we were able to locate low-lying Fisher's zeros by Chebyshev interpolations and residue theorem methods. On the small lattices, the scaling properties of the zeros are consistent with a second-order phase transition, while from the larger lattices there is some indication that this turns around and becomes consistent with a first-order transition.

Although $U(1)$ lattice gauge theory was already introduced in the pioneering paper by Wilson [56], it still resists to reveal clearly the true nature of its transition from the confinement to the Coulomb phase. Like other physical quantities, e.g., Polyakov loop susceptibilities, Fisher's zeros appear to need rather large lattices to display their asymptotic scaling properties. As modern supercomputers allow parallel processing on an unprecedented scale, the solution may finally become achieved by brute force calculations on very large lattices.

ACKNOWLEDGMENTS

This research was supported in part by the Department of Energy under Contracts No. FG02-91ER40664, No. DE-FG02-97ER41022, and No. DE-AC02-98CH10886. We thank C. Bender for pointing out the concept of Chebyshev ellipses and W. Jancke for providing unpublished figures of double-peak distributions in a case of second-order phase transition. The calculations were supported in part by a project of level C on the Fermilab cluster.

APPENDIX A: MULTICANONICAL DATA

The number of tunnelings and the integrated autocorrelation times for 4^4, 6^4, and 8^4 lattices is given in Tables X,

TABLE X. MUCA data for 4^4.

	MUCA 1	MUCA 2		MUCA 3	
#	N^{tunn}	N^{tunn}	τ_{int}	N^{tunn}	τ_{int}
1	1512	3886	99(2)	4697	110(1)
2	1406	4018	109(1)	2833	720(35)
3	1974	4723	114(5)	3492	540(15)
4	1552	4537	216(5)	2684	750(18)
5	774	5038	175(12)	4920	367(29)
6	963	4769	109(1)	5682	164(4)
7	196	397	1383(124)	3162	679(34)
8	4089	3875	101(5)	4547	116(5)
9	2344	4214	108(7)	4599	266(6)
10	1652	4582	185(15)	3484	625(48)
11	1622	4179	111(7)	5030	255(12)
12	1722	4281	126(3)	3985	674(101)
13	3406	4081	98(1)	4994	146(3)
14	1271	4127	104(6)	5257	135(6)
15	488	4610	255(9)	3776	524(14)
16	2351	4394	108(3)	4167	338(12)
17	788	4785	123(4)	4598	356(10)
18	735	4680	134(4)	4661	364(16)
19	845	4450	200(4)	3675	537(14)
20	2697	3526	93(1)	4123	104(7)

TABLE XI. MUCA data for 6^4.

#	MUCA 1		MUCA 2	
	N^{tunn}	τ_{int}	N^{tunn}	τ_{int}
1	1351	702(48)	950	559(27)
2	708	466(12)	897	480(11)
3	367	422(12)	947	502(17)
4	454	474(30)	971	561(31)
5	580	484(37)	894	565(47)
6	682	481(21)	911	511(23)
7	523	423(14)	909	557(43)
8	765	512(28)	903	532(33)
9	696	510(27)	921	485(12)
10	652	469(32)	935	569(53)
11	513	544(46)	976	523(33)
12	378	396(18)	976	536(27)
13	867	559(17)	961	495(10)
14	661	496(13)	932	509(28)
15	545	542(50)	896	554(38)
16	615	497(14)	920	496(13)
17	475	438(16)	979	543(46)
18	822	464(10)	903	486(11)
19	878	570(35)	892	508(30)
20	578	588(62)	949	572(28)

XI, and XII. Figure 16 illustrates the fluctuations among streams and the correlations among MUCA runs for the zeros on a 6^4 lattice. In Table XIII, we summarize the parameters of simulations on 10^4–20^4 lattices.

TABLE XII. MUCA data for 8^4.

#	MUCA 1		MUCA 2	
	N^{tunn}	τ_{int}	N^{tunn}	τ_{int}
1	145	1756(99)	252	1782(124)
2	79	1298(69)	240	1798(78)
3	75	1475(144)	259	2486(368)
4	121	1291(141)	216	2159(235)
5	150	2420(364)	216	1660(154)
6	86	1097(40)	256	1528(55)
7	74	1103(51)	255	1621(105)
8	132	1419(48)	254	1568(98)
9	187	3089(438)	197	3074(397)
10	98	1370(94)	255	1706(104)
11	142	1389(47)	208	1700(218)
12	165	1804(343)	254	1800(256)
13	93	1265(111)	270	1912(160)
14	212	2012(114)	231	1855(254)
15	137	1581(181)	249	1855(170)
16	159	1904(235)	211	1674(224)
17	269	1773(76)	213	2169(256)
18	206	1773(176)	234	1503(52)
19	214	1756(76)	212	1954(265)
20	96	1680(221)	227	1697(101)

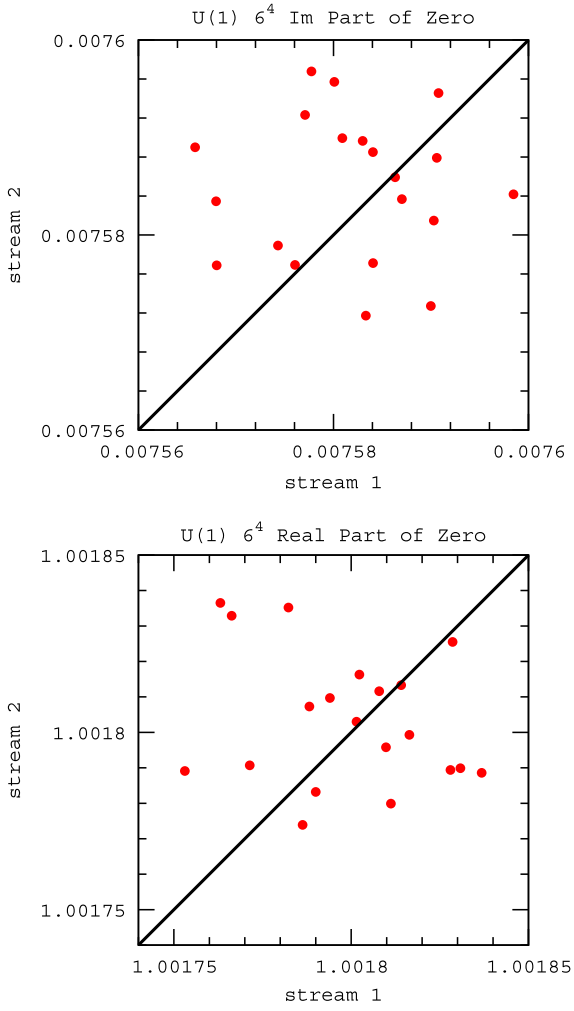

FIG. 16 (color online). Imaginary (top) and real (bottom) part of the complex zeros of MUCA run 1 versus MUCA run 2 for the 20 streams on a 6^4 lattice.

APPENDIX B: NUMERICAL DATA USED IN SEC. VII

In order to calculate the quantities used to make the graphs of Sec. VII, we have first fitted $f(s)$ in a region slightly wider than the location of the two peaks of $f(s) - \beta_S$ with the first 12 Chebyshev polynomials. Higher order polynomials tend to pick up the noise and provide results which are less stable. Using this polynomial

TABLE XIII. MUCA data for volumes where simulations were performed in narrow $[\beta_{\text{min}}, \beta_{\text{max}}]$ range. Last two columns summarize the number of tunneling events. 10^4–12^4 is from [54].

Volume	Sweeps	β_{min}	β_{max}	MUCA1	MUCA2
10^4	$32 \times 96\,000$	0.980	1.030	103	133
12^4	$32 \times 112\,000$	0.990	1.030	75	82
14^4	$32 \times 128\,000$	1.000	1.020	57	51
20^4	$64 \times 100\,000$	1.010	1.012	155	210

TABLE XIV. Numerical results described in the text.

L	β_S	s_1	s_2	$\Delta(f-\beta_S s)$	s_L	s_R	β_L	β_R	$\beta_R-\beta_L$
4	0.979 327	0.369 215	0.442 409	0.000 059752 7	0.384 952	0.425 551	0.976 759	0.981 792	0.005 032 62
6	1.001 76	0.352 413	0.410 538	0.000 053 319 7	0.364 762	0.395 541	0.998 768	1.004 46	0.005 693 44
8	1.007 38	0.348 089	0.394 932	0.000 033 706 4	0.358 049	0.382 876	1.005 04	1.009 51	0.004 472 97
10	1.009 42	0.345 567	0.386 254	0.000 023 194	0.353 401	0.375 09	1.007 47	1.011 03	0.003 562 33
12	1.010 22	0.345 633	0.380 806	0.000 016 449 5	0.352 382	0.370 685	1.0086	1.011 53	0.002 930 64
14	1.010 58	0.345 352	0.377 624	0.000 011 454 1	0.351 326	0.368 136	1.009 34	1.011 55	0.002 212 52
20	1.010 97	0.345 337	0.374 469	$7.154\,278\,2\ 10^{-6}$	0.349 468	0.362 23	1.009 88	1.011 57	0.001 691 1

approximation, we calculated the two roots of $f''(s)$ in the interval considered. We call them s_L (Left) and s_R (Right). They are the local extrema of $f'(s)$. The corresponding β [obtained from the saddle point Eq. (12)] are denoted β_L and β_R. For $\beta_L < \beta < \beta_R$, the saddle point Eq. (12) has three solutions instead of one (the "Maxwell kink"). β_S corresponds to the case where the area of the kink below and above are equal. The locations of the maxima of $f(s) - \beta_S s$ are called s_1 and s_2 as in Sec. V. $\Delta(f - \beta_S s)$ denotes the difference between the local minimum and the local maxima of $f - \beta_S s$. The numerical results are provided in Table XIV.

[1] T. Appelquist, G. T. Fleming, and E. T. Neil, Phys. Rev. D **79**, 076010 (2009).
[2] A. Hasenfratz, Phys. Rev. D **80**, 034505 (2009).
[3] Z. Fodor, K. Holland, J. Kuti, D. Nogradi, and C. Schroeder, Phys. Lett. B **681**, 353 (2009).
[4] A. Deuzeman, M. P. Lombardo, and E. Pallante, Phys. Rev. D **82**, 074503 (2010).
[5] Z. Fodor, K. Holland, J. Kuti, D. Nogradi, and C. Schroeder, Phys. Lett. B **703**, 348 (2011).
[6] A. Hasenfratz, Phys. Rev. D **82**, 014506 (2010).
[7] Y. Shamir, B. Svetitsky, and T. DeGrand, Phys. Rev. D **78**, 031502 (2008).
[8] J. B. Kogut and D. K. Sinclair, Phys. Rev. D **81**, 114507 (2010).
[9] T. DeGrand, Y. Shamir, and B. Svetitsky, Phys. Rev. D **83**, 074507 (2011).
[10] D. K. Sinclair and J. B. Kogut, Proc. Sci., LATTICE2010 (2010) 071 [arXiv:1008.2468].
[11] J. B. Kogut and D. K. Sinclair, Phys. Rev. D **84**, 074504 (2011).
[12] L. Del Debbio and R. Zwicky, Phys. Rev. D **82**, 014502 (2010).
[13] J. C. Myers and M. C. Ogilvie, J. High Energy Phys. 07 (2009) 095.
[14] T. DeGrand, Phil. Trans. R. Soc. A **369**, 2701 (2011).
[15] M. C. Ogilvie, Phil. Trans. R. Soc. A **369**, 2718 (2011).
[16] F. Sannino, Acta Phys. Pol. B **40**, 3533 (2009).
[17] B. A. Berg, Phys. Rev. D **82**, 114507 (2010).
[18] B. A. Berg, arXiv:1109.5861.
[19] A. Denbleyker, D. Du, Y. Liu, Y. Meurice, and H. Zou, Phys. Rev. Lett. **104**, 251601 (2010).
[20] Y. Meurice and H. Zou, Phys. Rev. D **83**, 056009 (2011).
[21] Y. Liu and Y. Meurice, Phys. Rev. D **83**, 096008 (2011).
[22] E. T. Tomboulis, Mod. Phys. Lett. A **24**, 2717 (2009).
[23] M. Fisher, in *Lectures in Theoretical Physics* (University of Colorado Press, Boulder, Colorado, 1965), Vol. VIIC.
[24] N. A. Alves, B. A. Berg, and S. Sanielevici, Phys. Rev. Lett. **64**, 3107 (1990).
[25] J. Jersak, C. B. Lang, and T. Neuhaus, Phys. Rev. Lett. **77**, 1933 (1996).
[26] J. Jersak, C. Lang, and T. Neuhaus, Phys. Rev. D **54**, 6909 (1996).
[27] W. Janke and R. Kenna, J. Stat. Phys. **102**, 1211 (2001).
[28] W. Janke and R. Kenna, Nucl. Phys. B, Proc. Suppl. **106–107**, 905 (2002).
[29] W. Janke, D. A. Johnston, and R. Kenna, Nucl. Phys. **B682**, 618 (2004).
[30] B. Klaus and C. Roiesnel, Phys. Rev. D **58**, 114509 (1998).
[31] I. Campos, A. Cruz, and A. Tarancon, Nucl. Phys. **B528**, 325 (1998).
[32] G. Arnold, T. Lippert, K. Schilling, and T. Neuhaus, Nucl. Phys. B, Proc. Suppl. **94**, 651 (2001).
[33] G. Arnold, B. Bunk, T. Lippert, and K. Schilling, Nucl. Phys. B, Proc. Suppl. **119**, 864 (2003).
[34] M. Vettorazzo and P. de Forcrand, Nucl. Phys. **B686**, 85 (2004).
[35] B. A. Berg and T. Neuhaus, Phys. Lett. B **267**, 249 (1991).
[36] F. Wang and D. P. Landau, Phys. Rev. Lett. **86**, 2050 (2001).
[37] A. Bazavov and B. A. Berg, Phys. Rev. D **71**, 114506 (2005).
[38] A. Bazavov and B. A. Berg, Comput. Phys. Commun. **180**, 2339 (2009).
[39] A. Denbleyker, D. Du, Y. Meurice, and A. Velytsky, Proc. Sci., LAT2007 (2007) 269 [arXiv:0710.5771.
[40] N. A. Alves, B. A. Berg, and R. Villanova, Phys. Rev. B **41**, 383 (1990).

[41] N. A. Alves, B. A. Berg, and S. Sanielevici, Nucl. Phys. **B376**, 218 (1992).
[42] L. Li and Y. Meurice, Phys. Rev. D **71**, 016008 (2005).
[43] A. Denbleyker, D. Du, Y. Liu, Y. Meurice, and A. Velytsky, Phys. Rev. D **78**, 054503 (2008).
[44] R. Balian, J. M. Drouffe, and C. Itzykson, Phys. Rev. D **19**, 2514 (1979).
[45] C. Michael and M. Teper, Nucl. Phys. **B314**, 347 (1989).
[46] R. Horsley and U. Wolff, Phys. Lett. **105B**, 290 (1981).
[47] Y. Meurice, Phys. Rev. D **74**, 096005 (2006).
[48] C. Borgs, R. Kotecký, and S. Miracle-Solé, J. Stat. Phys. **62**, 529 (1991).
[49] C. Borgs and R. Kotecký, J. Stat. Phys. **61**, 79 (1990).
[50] A. Billoire, T. Neuhaus, and B. Berg, Nucl. Phys. **B396**, 779 (1993).
[51] J. P. Boyd, J. Sci. Comput. **3**, 109 (1988).
[52] P. Kravanja, M. Van Barel, O. Ragos, M. Vrahatis, and F. Zafiropoulos, Comput. Phys. Commun. **124**, 212 (2000).
[53] B. Berg, *Markov Chain Monte Carlo Simulations and their Statistical Analysis* (World Scientific, Singapore, 2004).
[54] B. A. Berg and A. Bazavov, Phys. Rev. D **74**, 094502 (2006).
[55] H. Behringer and M. Pleimling, Phys. Rev. E **74**, 011108 (2006).
[56] K. G. Wilson, Phys. Rev. D **10**, 2445 (1974).